

Title: Deployment of an electrocorticography system assisted with a soft robotic actuator

Authors: Sukho Song^{1,2}, Florian Fallegger¹, Alix Trouillet¹, Kyungjin Kim^{1,3}, and Stéphanie P. Lacour^{1†}

Affiliations: ¹ Bertarelli Foundation Chair in Neuroprosthetic Technology, Laboratory for Soft Bioelectronic Interfaces, Institute of Microengineering, Institute of Bioengineering, Centre for Neuroprosthetics, École Polytechnique Fédérale de Lausanne (EPFL), 1202 Geneva, Switzerland.

² Laboratory of Sustainability Robotics, Swiss Federal Laboratories for Materials Science and Technology (Empa), 8600 Dübendorf, Switzerland.

³ Department of Mechanical Engineering, University of Connecticut, Storrs CT 06269, United States

†Correspondence to: stephanie.lacour@epfl.ch

Abstract:

Electrocorticography (ECoG) is a minimally invasive approach frequently used clinically to map epileptogenic regions of the brain and facilitate lesion resection surgery, and increasingly explored in brain-machine interface applications. Current devices display limitations that require trade-offs between cortical surface coverage, spatial electrode resolution, aesthetic, and risk consequences, and often limit the use of the mapping technology to the operating room. In this work, we report on a scalable technique for the fabrication of large-area soft robotic electrode arrays and their deployment on the cortex through a square centimeter burr hole using a pressure-driven actuation mechanism called eversion. The deployable system consists of up to six pre-folded soft legs and it is placed subdurally on the cortex using an aqueous pressurized solution and secured to the pedestal on the rim of the small craniotomy. Each leg contains soft, microfabricated electrodes and strain sensors for real-time deployment monitoring. In a proof-of-concept acute surgery, a soft robotic electrode array was successfully deployed on the cortex of a minipig to record sensory cortical activity. This soft robotic neurotechnology opens promising avenues for minimally invasive cortical surgery and applications related to neurological disorders such as motor and sensory deficits.

One-Sentence Summary: We combined soft robotic actuation with bioelectronics to develop minimally invasive, deployable cortical electrode arrays.

This document is the accepted manuscript version of the following article:

Song, S., Fallegger, F., Trouillet, A., Kim, K., & Lacour, S. P. (2023). Deployment of an electrocorticography system with a soft robotic actuator. *Science Robotics*, 8(78), eadd1002 (12 pp.). <https://doi.org/10.1126/scirobotics.add1002>

INTRODUCTION

Electrocorticography (ECoG) grids are a class of surface electrode implants used to investigate neural activities across large areas of the brain (1-4). ECoG grids find a wide variety of applications in basic neuroscience and clinical settings including brain function monitoring (5-8), alleviation of epileptic seizure (9), brain function recovery (10, 11), pain modulation (12), speech recognition (13) and brain-computer interfaces (BCI) (14). The large area coverage of ECoG grids is especially useful in investigating neurological disorders associated with several regions of the brain, such as spreading depolarizations after traumatic brain injury (4, 15, 16). However, challenges arise when implanting grids with large surface areas (such as $> 10 \text{ cm}^2$) over the cerebral cortex.

Conventional research and clinical ECoG grids are mechanically passive devices, which are surgically laid over the cortex following a craniotomy that exposes the brain (17). The size of the craniotomy is at least as large as the footprint of the ECoG grid (in some cases, smaller ECoG strips may be inserted below the skull). Neural recordings are usually performed intraoperatively or over short periods of time (< 30 days) during which the patient remains at the hospital. A cranioplasty using autologous skull or synthetic materials completes the procedure. The large craniotomies are often a limiting factor in the use of ECoG grids, considering both the risk-benefit ratio and acceptability of the procedure by the patients. Post-surgical complications may arise including inflammatory response and scarring, morphological changes on the brain, and neurological deficiencies (18-21). An alternative to such planar ECoG grids is stereotactic electroencephalography (sEEG) probes that are implanted through small burr holes ($< 1 \text{ cm}^2$) in the skull thereby having a lower risk profile than ECoG (22).

In this work, we propose a deployable ECoG system, assisted with soft robotic actuation, to surgically implant large area and soft microfabricated ECoG grids on the cortex through small burr holes. The deployment approach relies on a bio-inspired, soft robotic mechanism called eversion (23). The ECoG grid is prepared with the soft micromachining process enabling thin ($< 400 \text{ }\mu\text{m}$ thick), dura mater-like electrode implants (24).

Eversion is an actuation mechanism that relies on the deployment of initially inverted, structurally cylindrical thin-walled sleeves. When pressurized, the sleeves flip inside out, elongate, and move forward. It has been used in a wide variety of different applications ranging from medical catheters (25) to frictionless rubber seals in a rolling diaphragm cylinder (26). The mechanism has recently been re-discovered by Hawkes et al. and used it as a bio-inspired soft robot that can 'grow' longitudinally, squeeze through small openings and explore constrained environments (27-30).

Here, we developed a soft robotic ECoG system utilizing eversion actuation as a deployment mechanism for large surface areas. The system also implemented with built-in strain sensors, which monitor, in real-time, the deployment of the soft implant under the skull. The sensors provided critical feedback on when to stop the everting motion. The micromachined elastomeric sleeve with hydrophilic inner surface allowed controlled eversion through pressurized dispensing of a biocompatible lubricant, such as saline solution. Furthermore, the entirely soft, thin-walled everting ECoG system ensured an intimate contact to the curvilinear brain surface. Finally, an in-vivo demonstration showed full functionalities of the proposed ECoG system through eversion, deployment sensing, and acute neural recording of a mini-pig model.

RESULTS

Design and fabrication of the deployable ECoG system

The eversion mechanism, strain sensor, and neural electrodes were combined into a single deployable ECoG system using soft micromachining process (**Fig.1A**). Two planar elastomeric membranes made of Polydimethylsiloxane (PDMS) were stacked to form the implantable interface. The inner surface of the PDMS-made implant was treated to be hydrophilic (**Fig.S1C-D**), enabling lubrication with biocompatible aqueous fluids. The first membrane hosts the microelectrode arrays and strain sensors (24) prepared with the silicone-on-silicon process (31),

and displays natural dura mater-like compliance. Metallic tracks (**Fig.1B-iii**) were thermally evaporated (35-nm-thick gold thin film) on top of the elastomer surface to form microcracked elastic interconnects that sustain stretch over 30 % strain without electrical failure (24, 32). Electrode sites were coated with a Platinum (Pt)-PDMS composite that establishes an intimate contact with the nervous tissue to support low electrical impedance, and mechanical compliance (**Fig.1B-ii**) (33). Resistive strain sensors were prepared on the elastomeric substrate with similar microcracked gold thin film (34). The second membrane of plain silicone was bonded at the edge of the first membrane using a soluble sacrificial layer as a spacer and completed the leg-shaped tubular stack. A thin flexible printed circuit board was integrated with the interconnects to form a low geometrical profile connector. The detailed fabrication process is available in the method section and supplementary information (**Fig. S1**).

Fig.1B shows a photograph of a soft ECoG system containing six actuated legs (6 mm wide and 0.4 mm thick) (**Fig. 1B-i**). Each leg contains four interconnects, associated microelectrodes (red in **Fig. 1B-i**) surrounded by a strain sensor patterned on the outer contour of the deployable strip (green in **Fig.1B-i**). In preparation for surgical implantation, the ECoG system is secured to a loader connector using a thin layer of Vinylsiloxane silicone elastomer providing a temporary seal between the array and the loader (**Fig. S2**). Biocompatible aqueous solution (such as saline, phosphate buffer solution (PBS), or Dextran solution) is used as a lubricant to reduce layer friction inside the soft ECoG system during folding and deployment.

Next, the ECoG legs were folded into the 20 mm diameter loader (**Fig.1C-E**) that matched typical 20 mm burr holes. The rigid loader was positioned on the cranium, immediately above the preliminary drilled circular burr hole. **Fig.1E-i** shows the three-step deployment process within a hydrogel phantom human brain (Agarose, 0.5 wt %) and a transparent plastic (PET) skull. A positive fluidic pressure differential is applied inside the loader, increasing the fluidic force F at the everting tip (**Fig.1C-i**). The array stays folded until the fluidic force overcomes friction f with respect to the increase in the positive fluidic pressure differential. When the fluidic force becomes greater than the friction, the folded array is gently pushed out of the tip via eversion by flipping inside-out, and extends under the stiff skull (**Fig. 1C-ii**). As the eversion creates new volume to lengthen the array from the tip, the fluidic pressure differential drops. The tip growth stops as the fluidic pressure becomes smaller than the friction and until the pressure differential increases sufficiently enough to reiterate the above cycle. Note that the highest-pressure differential for deployment remains constant for a given leg cross-section (mm^2 range) independently on its length, which is one of the main advantages of the pressure-driven eversion.

A mechanical support made of 50 μm thick polyimide (PI) film prevents the circular PDMS diaphragm at the center of the soft ECoG system from inflating and compressing the brain by bulging out with the positive pressure differential. **Fig. 1D-ii** shows a 40 mm diameter, fully deployed implantable system. During deployment, which typically lasts thirty to forty seconds per leg (**Movie S1**), the inflated legs can slightly push against the brain. The resultant compressive strains are discussed in the next section. Once the system is fully deployed and depressurized, the high compliance (Young's modulus, E approximately 700 kPa) and low profile (thickness, h approximately 0.4 mm) of the deployable ECoG grids allow intimate contact with the surface of the brain with improved conformability to existing clinical ECoGs (**Fig. S3**). After the ECoG monitoring, the deployed grids could be easily pulled out from the brain, similarly to non-deployable implants (31).

Structural characterization of the soft ECoG system

Implementing pressure-driven eversion within the subdural cortical space calls for minimal compression of the underlying brain tissue. To do so, we first investigated the shape and geometrical parameters of deployable legs, namely the leg width w , thickness h on straight single legs (**Fig. 2A-i**), the taper angle a on tapered legs (**Fig. 2A-ii**), and the radius of curvature r_c on curved legs (**Fig. 2A-iii**). Deployment characterization was performed using compressed air to readily monitor the air pressure differential P_a inside structural prototypes as the pressure

gradually increased then suddenly dropped at the moment of deployment. We defined the metric P_d , for deployment pressure, as the maximum of air pressure differential to quantitatively evaluate the deployability of each design (**Fig. 2B**). The highest P_d indicates the most difficult design to deploy. **Fig. 2C-i, ii** and **Movie S2** display the deployment of two distinct leg geometries with the tapered and curved configuration. The width and thickness, w and h , of straight legs notably affected P_d during deployment (**Fig. 2D-i**): P_d increased as the leg narrowed and thickened. In the present design, P_d increased by 2.8 times regardless of the width w if the thickness h is doubled. On the other hand, the taper angle (curvature) affected minimally P_d and the leg deployability (**Fig. 2D-ii** and **iii**). Increasing the curvature of the legs was of particular interest as larger surface coverage may be reached (**Fig. 2A-iii**, **Movie S3**). P_d stayed nearly constant, at 10.4 kPa on average regardless of r_c ranging from 6 mm to 30 mm, showing that r_c did not have any substantial effects on P_d (**Fig. 2D-iii**).

Upon pressurization, each leg inflated with oval cross-sections owing to its rectangular relaxed shape. Such inflation may locally and momentarily compress the underlying brain. To quantify the resulting displacements, we measured the local strain maps in phantom brain models using a digital image correlation (DIC) technique and computed them using finite element modeling (**Fig. 3**). The cross-sectional shape of the inflated leg evolved from oval to circular with increasing deployment pressure P_d (**Fig. S4A**). The circumferential elongation of the leg envelope remained negligible until the circular shape appeared with high enough P_d (**Fig. S4A-iii** and **Fig. S4A-iv**). Such large radial expansion was however not observed for legs with $h < 0.4$ mm and 4 mm $< w < 8$ mm.

To quantify eventual brain compression upon pressurization of the leg, we designed a mock system of the brain and cranium using a soft hydrogel brain model (Agarose, 0.5 wt %, $E \sim 5.3$ kPa (35)) and a stiff plastic frame, respectively. The brain and skull models are 1 mm apart, accounting for the epidural space (side-views in **Fig. 3A**). The gel was coated with randomly dispersed graphene nanoplatelets to allow for displacement tracking. A straight leg prototype ($h = 0.4$ mm and $a = 0$ deg) was inserted in the gap and pressurized to the deployment pressure P_d defined in **Fig. 2D-i** (**Movie S4**). Upon pressure, the cross-section of the soft leg changed its shape from flat to oval thereby compressing the hydrogel brain model (front-views in **Fig. 3A**). The resulting density of the graphene nanoplatelets increased in the vicinity of the inflated leg (front-view in **Fig. 3A-ii**). **Fig. 3B** displays maps of vertical displacement of the hydrogel brain model computed from the tracked displacement of the carbon suspension (36). The resulting indentation d_i on the surface of the brain model was defined as the vertical displacement of the graphene nanoplatelets referenced to their initial configuration (solid and dashed lines, respectively in front-views in **Fig. 3A-i** and **Fig. 3A-ii**). The center of the coordinate system (or the origin) of the indentation map was defined at the bottom center of the inflated leg as shown in **Fig. 3A-ii** and **Fig. 3B**.

Fig. 3C displays d_i along the z -axis ($x = y = 0$) as a function of the hydrogel depth z for different leg width w (5 mm $< w < 8$ mm). The gel displacement d_i was maximal $d_i = d_{\max}$ immediately below the central axis of the leg ($x = y = z = 0$), and reached to plateaus to about 0.6 mm at a depth of about 6 mm independent on the leg width (**Fig. 3C**). Wider legs induced larger overall displacement of the underlying gel ($d_{\max} = 1.7$ to 2.5 mm for $w = 5$ mm to 8 mm, respectively), although its slope became smaller with the increase in leg width, also predicted by the FEM model (**Fig. 3D**). This may be explained as wider legs can be deployed with a smaller P_d thereby inducing lower compression on the brain phantom. The experiments and simulations were in good agreement, with overall deviation of only 0.06 mm from the average of the measured d_{\max} .

With the verified model, we estimated the effect of reduction in device thickness on the indentation of the cortex. We numerically calculated d_{\max} of leg strips with half the thickness ($h = 0.2$ mm), compared to the experimentally tested legs ($h = 0.4$ mm). The 0.2-mm-thick leg strip in the FEM model was inflated virtually with its corresponding P_d measured in **Fig. 2D-i** (**Fig. 3E**). d_{\max} for the 0.2-mm-thick leg strip (dotted line) showed approximately 0.6 mm less indentation on average than d_{\max} for the 0.4 mm-thick leg strip (dashed line). This decrease in d_{\max} was attributed to the prompt eversion associated with 2.8 times smaller P_d for the thinner

legs. Note that this FEM model computes d_{\max} based on P_d when the implantable system is deployed in an unconstrained environment. The computed d_{\max} values are therefore underestimated. This is due to factors such as poor lubrication, a reduced gap between the brain and the skull, adhesion between the skull and the dura mater in case of epidural implantation, or high curvature of the skull, can increase P_d (see the effects of the increased P_d on d_{\max} as shown by the colored solid lines in **Fig. 3E**).

Proof-of-concept of the soft ECoG system in-vivo

Next, we investigated the potential of the deployable ECoG system in-vivo to record cortical brain activity acutely in a minipig model. Geometrical features of the minipig's brain (such as curvature of the brain) are close to that of the human brain (37). Design considerations were made to limit the indentation on the cortex as small as 2 mm. This dimension proved to be a safe limit in human brain surgeries (38). The system also needs to be deployed with minimal fluidic pressure in order to permit slow and less invasive eversion. We developed an implantable soft ECoG prototype with a straight single leg with a size of 6-mm-width, 0.4 mm thickness, and 15 mm length that satisfies the above design criteria. The estimated indentation depth is approximately 2 mm based on the data in **Fig. 3** with the lowest deployment pressure among possible design options. The 15 mm leg strip is long enough to target the rostrum somatosensory cortex, when deployed from top of the brain.

Photographs of the folded (pre-implantation) and deployed soft ECoG are shown in **Fig. 4A**. The deployable system supports a 3x4 electrode array (0.3 mm diameter, 1.5 mm center-to-center pitch) with metallic interconnects and a strain sensor (**Fig. 4A-iii**) that are made of microcracked gold thin film (**Fig. 1B-iii**) (24). The strain sensor surrounds the array and allows real-time monitoring of the status of the leg deployment. Firstly, the implant was folded within the holder using a small plastic rod (**Movie S5**). Here, ethanol lubricated the contact surface between the ECoG leg strip and the plastic rod. The lubricant evaporated quickly from the leg surface and disappeared shortly after the plastic rod was removed before the in-vivo use. The initial resistance R_o of the strain sensor (in its flat form) was approximately 10 k Ω and increased up to several mega-ohms upon folding (**Fig. 4B**). The resistance after folding R_f remained in the M Ω range during deployment with an increasing P_d and recovered its initial low value once the array laid flat (**Fig. 4C**, $R_d < 15$ k Ω at $t > 27$ s, **Movie S5**). Although there were two orders of magnitude difference in electrical track resistance between R_f and R_d , the resistance after deployment R_d remained constant following 50 cycles of repetitive folding and deployment (**Fig. 4D**), indicating the microcracked gold film sustains such demanding mechanical loading. **Fig. 4E** shows that folding and deployment also had minimal effect on electrochemical impedance of the electrode sites, confirming their robustness to extreme deformations. Instead of using compressed air, deployment could also be induced by incompressible fluid medium (Dextran 15wt % in this case), which resulted in slower deployment speed (**Fig. 4F**). The incompressible aqueous solution filling the entire deployment system prevents building of the pneumatic energy compared to the compressed air, which leads to fast and uncontrolled deployment (**Fig. S5** and **Movie S6**).

In-vivo validation of the soft ECoG system

We demonstrated the in-vivo deployment and recording capability of the soft ECoG system via eversion in an anesthetized Göttingen minipig model. The model possesses a large gyrencephalic brain with a vascular density and skull thickness similar to humans (39). We recorded somatosensory evoked potentials (SSEPs) at the surface of the brain in response to the electrical stimulation of the snout. A single-legged, straight ECoG strip (**Fig. 4A**) was deployed subdurally at the surface of the cortex targeting the frontal lobe and the somatosensory region. The dimensions of the soft implant supported a deployment from the superior part of the skull thus did not require a craniotomy above the central sinus vein or displacement of the temporal muscle laterally.

The deployable ECoG system was first filled from the inside with PBS and was folded using a plastic rod with ethanol as shown in **Movie S5**. Following complete ethanol evaporation, the folded array was thoroughly rinsed again with PBS to make sure that there will be no ethanol residue in contact to the brain. Following durotomy (**Fig. 5A-i**, see Methods for details), the loader was placed at the surface of the brain. The base of the device was placed in contact with the cortex, at the frontal edge of the craniotomy with the folded leg facing the anterior section (**Fig. 5A-ii**). A syringe pump was used to inject PBS into the loader to initiate and control the subdural deployment. The strain sensor output indicated when the soft leg was fully deployed ($R_d = 21 \text{ k}\Omega$ at $t = 42 \text{ s}$, **Fig. 5B**). Next, the loader was removed, and the implant was electrically connected to the electrophysiology recording system.

We recorded evoked potentials from the somatosensory cortex induced by electrical stimulation of the snout delivered at three distinct locations of the snout and two stimulation amplitudes (**Fig. 5C-i**). Averaged signals from selected channels presented depolarization and polarization peaks (**Fig. 5C-ii and iii**) and a timing similar to previous reports for SSEPs (40). The SSEPs with amplitudes reaching $>30\mu\text{V}$ peak amplitude displayed location-specific characteristics of amplitude and waveform that were consistent with a spatial map of the snout representation (41). The position of the deployed array on the somatosensory area was confirmed post-mortem (**Fig. 5D**) (37). The soft implant did not present any folded part and conformed well with the cortical surface (**Fig. 5E-i to iii**). No visible damage was evident under or in the vicinity of the deployment location after whole brain extraction. In particular, morphological change or ruptured tissues due to the deployment of the everting strip were not visible (**Fig. 5E-iv** and **Fig. S6**). Post-mortem histochemistry was also performed to further analyze inflammation and neuronal health. Coronal sections were stained using three markers, Iba1 GFAP and NeuN, for microglial cells, astrocytes and neurons, respectively at 3 different locations under the implanted zone corresponding to base, stem, and tip of the deployed ECoG (**Fig. S7A**). Cross-sectional images confirmed that there was no visible damage outside and under the implanted zone and no indentation of the brain, suggesting the eversion-based deployment was indeed soft and gentle to the brain tissue as designed (**Fig. S7B, F**). At the microscopic level, sporadic microglial activation was noticed in the vicinity of the base and the stem (zones **i** and **ii**, **Fig. S7E-i, ii**), but not in the tip (zone **iii**, **Fig. S7E-iii**). No notable glial cell reaction (**Fig. S7E**) and limited astrocytes proliferation were observed (**Fig. S7C**). In addition, neuron imaging showed intact cortical layers (**Fig. S7D**), except for the stem that displayed some loss of neurons on a limited part under the implanted zone (**Fig. S7B-ii**). Note that no glial cell activation, astrocytes proliferation, and neuronal loss were observed in the tip where the cortical tissue sustains lower compression than that at the implant base (lower form factor of the implant rounded tip). Although multiple factors (such as indentation depth and deployment speed) can contribute to the damage mentioned above, this result suggests that minor modifications to the current design, such as thinner or narrower legs, may be sufficient to ensure the safety of the implanted brain at a microscopic level. These are initial observations from an acute test ($N = 1$) that will need consolidation across a larger number of animals and longer timepoints.

DISCUSSION

Conventional ECoG grids are mechanically passive devices and are used clinically in conjunction with extensive craniotomies that expose the cortex over areas typically at least as large as the size of the neural interface. Various adverse effects can be associated with large craniotomies including high risk of infection, possible brain damage as well as aesthetic impairments of remaining large scars (20). These risks substantially limit the adoption of ECoG arrays for large-scale functional brain mapping or permanent cortical implants for brain machine interfaces.

To mitigate these effects, minimally invasive deployment methods for ECoG arrays have been recently explored. Thin implants can be steered and positioned on the rat cortex using a pair of magnets across the skull (with one external magnet and another one embedded in the

implant) (42). However, the translation to the human skull that is eight times thicker than that of rodents is challenging (43, 44). Woodington, et al. leveraged microfluidic actuation to unfold a thin, rolled electrode paddle at the surface of the spinal cord of a human cadaver (45). The unfurling actuation however requires pre-insertion of a rolled-up paddle on the brain or on the spinal cord before deployment, which may result in greater pre-insertion depth and a larger craniotomy proportional to the array size.

The brain is the softest organ of the body (46, 47) and insertion into its structure may lead to catastrophic consequences for neuronal network activity and overall brain function. Robotic deployment of the soft ECoG in the epidural space – a constrained gap between the skull and the cortex – should be highly controlled. Periodic variations in arterial blood pressure during cardiac cycle and respiration are accompanied with constant motion of the brain (48), which further calls for soft, biomimetic designs that may trigger limited adverse immune responses and tissue damage (49-51).

Here we leverage soft robotic designs and soft bioelectronic devices to propose an implantable system that answers needs in terms of safety, cortex coverage and electrophysiologic sensing. The fluid-based eversion can produce sufficient actuation force to deploy the implant in the subdural space. The eversion-based ECoG system retains the folded strips outside the skull and maintains a low thickness profile during deployment on the final surface area of the implant, which provides a critical advantage over other deployment mechanisms for large electrode areas. The folded strips are fed from a loader situated outside the skull through a burr hole. Therefore, a larger surface area of the deployed electrodes requires only a bigger loader without increasing the size of craniotomy or the compression depth on the brain (**Fig. S8**). Furthermore, the everting ECoG system is entirely developed from a soft and biocompatible elastomer with Young's modulus less than 1 MPa, which is comparable to that of the biological dura mater (24).

An important consideration in the design of the deployable ECoG is its insertion and deployment over the largest possible surface area. Hawkes et al. demonstrated that eversion has no limit on the length of deployable strip through a given hole size (29). This implies that the eversion-based deployment system could ideally cover the entire cortex area using a large size loader through a tiny burr hole suitable for just a single curved strip (**Fig. S8B**). Trade-offs between the deployment pressure, geometry and electrode density is however needed, before applying the above scenario to a practical application. For example, reducing the number of legs requires increasing the integration density drastically (such as connection pitch to electrically connect the metallic interconnect to the FPCB cable). Therefore, the multi-legged configuration in **Fig. 1B** should be chosen over the single curved leg design presented in **Fig. S8B**, if the number of electrodes on the implant increases. Additionally, the deployment pressure can be substantially reduced by reducing the thickness of the soft substrate (**Fig. 2D-i**), which will lead to a smaller indentation of the brain during implantation. Other design strategies, such as increasing the number of strips while reducing leg width or incorporating variable leg curvature along the leg length, also need to be considered to reach the final implant design (**Fig. S9**). Overall, further advances in thin-film manufacturing and packaging technology in conjunction with the shape optimization discussed above will enable improved soft robotic ECoG arrays for human neurosurgeries (52) with higher area coverage and larger safety margin than the devices shown in this work as a proof-of-concept.

'Proprioception', the ability of self-awareness to its body motion, is a critical and important concept for a robotic device but has never been demonstrated by any previous deployment systems for neural implant. The proposed soft ECoG system includes a built-in sensor informing in real-time on the status of deployment. This is enabled through thin metallic film strain sensors that are integrated within the process flow of the implantable system. The use of resistance change of conductive elastomer composites or liquid metals has prevailed as strain sensors for the purpose of touch or motion sensing of various wearable and soft robotic devices (53-57). Here we leverage the strain sensitivity of thin gold film for in situ and real-time deployment detection. Inversion or full eversion of the deployable ECoG strip leads to a substantial change in track resistance of the microcracked gold strain sensor, which nevertheless

displays reproducible performance up to 50 reversible loading cycles (**Fig. 4D**). Unlike medical imaging tools (such as fluoroscopy) requiring manual intervention from a human surgeon for controlled deployment, the strain sensor can easily be incorporated into a closed-loop feedback control system to precisely manipulate a pressure source to increase, decrease, or to stop the pressurization of the deployable ECoG system automatically.

Here, we have shown that by combining soft robotic actuation, proprioceptive sensing and soft bioelectronic neurotechnology, we can engineer an implantable soft robotic neural interface that answers requirements for minimally invasive implantation of large area electrode arrays with customized electrode layout. In-vivo acute brain recording of minipig's SSEPs measured typical local field potentials which amplitudes and timings were similar to previous reports (40). No visible morphological damages could be observed after implantation (**Fig. 5**). However, local microscopic damages shown in the histochemistry analysis (**Fig. S7**) call for further optimization towards biosafety of the deployment system. Future works replicating these initial findings will assess further the surgical procedure, design and suitability of the deployable system as a chronic neurotechnology. Usability aspects also need to be optimized for a more straightforward use in the surgical theater, such as improvement on the securing and removal of the loader connector. Further advances in soft electrode manufacturing should be developed to miniaturize the soft ECoG array and enable the concept of multi-legged and curved deployment systems with high area coverage.

The concept of leveraging complementary fields of soft robotics and soft bioelectronics in this work can find applications beyond that of soft neurotechnology (58-62) as the leg and electrode designs may be adapted for specific geometric constraints and targeted organs. For example, deployment over the heart will allow the epicardial mapping of the electrical activity for the diagnosis of atrial fibrillation with much more coverage and precision than current catheter-based solution (63). Also, the ability to deploy a large electrode array through a small opening can also be leveraged in laparoscopic surgeries in mapping bowel, renal or liver electrical activity (64, 65). Furthermore, spinal cord stimulation electrode arrays (45, 66) can be inserted using a single leg design, while minimizing the size of spinal cord exposure of the conventional open surgery or dual laminectomy (24). The proposed soft robotic neural interface opens promising avenues for the development of accessible and minimally invasive surface implants for patients. Improved safety and usability of the soft CoG system will find a wide range of possible applications from the treatment of various neurological disorders.

Materials and Methods

Study design

The main objective of this study is to combine soft robotic sensing and actuation mechanism called eversion with implantable soft microelectrode arrays for minimally invasive electrocorticography. Experiments in this study were designed to characterize the effect of various design parameters on the system performance and to validate the proposed functionalities of the implant as follows. The deployment pressure was measured five times ($N = 5$) for each deployable ECoG strip design corresponding to a different combination of design parameters in leg width, thickness, taper angle, and radius of curvature. The indentation of the hydrogel blocks was measured three times ($N = 3$) for each straight ECoG strips ($h = 0.4$ mm) with four different leg widths ($w = 5, 6, 7$, and 8 mm). The electrical track resistance of the strain sensor was measured by folding and unfolding a single-legged ECoG array for 50 times. The electrochemical impedance spectroscopy of electrode sites and gold interconnects were performed on 10 working electrode sites ($N = 10$). Finally, the measurements of deployment speed were performed five times ($N = 5$) on a straight ECoG strip ($h = 0.4$ mm, $a = 6$ mm, and $w = 6$ mm) filled with two different fluid media conditions at three different syringe pump speeds (40, 120, and 240 mL/hr). All experiments were performed more than three times ($N > 3$) to estimate mean value and standard deviation of each measurements. Also, there was

no specific treatment of outliers and all measured data were included. Detailed information about measurement techniques can be found in the supplementary materials.

Fabrication and experimental methods

Both functional and structural samples of deployable ECoG systems were made of medical grade Polydimethylsiloxane (PDMS) elastomer (LSR M130, Elkem Silicones) based on the Silicone-on-Silicon (SoS) process established in our previous work. Samples prepared for structural characterization were fabricated without the interconnects and Pt-PDMS electrode coatings. According to our experiments, PBS (pH 7.4, Gibco) washes out the Dextran coating inside the deployable ECoG strip deposited in the process **Fig. S1E** over multiple folding and deployment. The PDMS surface inside the deployable ECoG tube returns from hydrophilic to hydrophobic that cannot be lubricated with the aqueous solution anymore. Therefore, those structural samples were filled with 15 wt% Dextran solution serving as a lubricant for long-term and repetitive eversion. In case of the functional deployable ECoG strip equipped with electrodes and interconnects for *in-vivo* testing, on the other hand, the sample was filled with PBS to achieve the maximum biocompatibility with the brain tissue for a few times of eversion within a short period. Please see the “Fabrication methods” as well as “Experimental methods” sections in the Supplementary Materials for a complete description.

Methods for in-vivo acute neural recording

Surgical procedures were approved by the local ethical committee in accordance with the guidelines for the Care and Use of Laboratory Animals and approved by local (Canton of Geneva) and federal (Swiss) veterinary authorities with authorization number GE11120A. The single-legged deployable soft robotic ECoG array shown in **Fig. 4A-i** was used for the *in-vivo* experiment. A Göttingen minipig of 8.5kg (3 months old) was anesthetized with a pre-medication mix of azaperone (0.4mg/kg), midazolam (0.75mg/kg) and atropine (0.2mg/ml) and induced with 6% sevoflurane. After intubation an intravenous line is placed on the ear for continuous administration of 10mL/h propofol at 2%wt and along a bolus of 2 μ g/kg fentanyl during the heavy surgical procedures. The surgery is performed as following: A large frontal to posterior incision is made over the midline. The muscle is retracted, and the periosteum is removed using an elevator. The midline and bregma are identified. The craniotomy is planned 2mm laterally from the midline to 20mm and -10mm to +20mm anterior to frontal. The skull is drilled with a neurosurgery drill (Bbraun Elan 4 using a 2.5mm neuro cutter drill bit) until reaching the dura. Then the boneflap is broken free using a spatula. The dura mater is incised with a microscalpel (stab scalpel knife, Fine Science Tools) in a U-shape away from the midline. The dura mater is placed towards the midline and kept hydrated. The loader system with the soft robotic ECoG array, filled with 15% Dextran, is placed at the frontal edge of the craniotomy and kept in place using a bench stand. The soft robotic ECoG array is deployed by using the linear syringe pump and electrical resistance of the strain sensor is monitored with the microcontroller using the customized LABVIEW Code. After the deployment, the sensory evoked potentials are elicited using bipolar needles inserted in the snout (2mm inside the skin) and stimulated with an isolated pulse generator (Isolated pulse generator 2100, AM Systems) at 5 and 10mA, symmetric, cathodic first, biphasic pulses with 300 μ s pulse width at 2Hz repetition rate. The brain signals were acquired by connecting the FPCB on the implant to a custom printed circuit board connected to a wireless head stage amplifier system (Multichannel Systems Wireless W2100). A ground wire is inserted epidurally on the contralateral side. The acquisition is performed at a sampling frequency of 2kHz with a digital Butterworth bandpass filter of 1–200 Hz and a notch filter at 50Hz. The recorded signals were averaged over each individual stimulation pulse for a total of 30s (roughly 60 epochs per condition). The experiment was performed for different stimulation pulse amplitudes (baseline, 5mA and 10mA) for the three snout stimulation positions. After the recordings, two catheters were inserted in the right jugular aorta vein, and the animal was sacrificed using 5mL of pentorbital injected in IV. Then 1L of 0.1M phosphate buffered saline with heparin (100'000 units for 1L) was injected at 200mL/min using a peristaltic pump (Shenzhen LabS3/UD15) followed by 5L of a PBS solution containing

4% paraformaldehyde at 200mL/min. After the perfusion, the animal was decapitated using a scalpel knife by incising the skin, muscle and between the first and second vertebrae. The head was then post-fixed in 4% PFA solution for a few days. The brain with the deployed soft robotic ECoG array was then extracted by removing first the skin and muscle using a scalpel knife, then the bone using bone rongeurs. The dura mater was carefully incised to reveal the deployment status of the implant. Finally, after removal of the device the whole brain was extracted from the skull cavity.

Methods for post-mortem histochemistry

The explanted brain was post-fixed in 4% PFA solution for 48 hours before the hemispheres were separated using a scalpel knife. Then parallel cuts were made at the front and back of the implantation area to isolate a block for further sectioning. The block was immersed in 15%wt then 30%wt sucrose solution for 3 days, respectively. The brain block was then frozen in isopentane at -55°C in a tissue freezing system (Excilone Snapfrost). The frozen brain was then sliced in 40µm sections using a cryostat (Leica CM1950). Immunostaining was then performed on several sections covering the entire zone of implantation. After incubation in Triton 0.3% and BSA 3%, tissues were incubated with primary antibodies for 48 hours at RT (Anti-GFAP, Rat, ThermoFischer, # 13-0300, Anti Iba1, Rabbit, FujiFilm, 019-19741, Anti-NeuN, GuineaPig, SigmaAldrich, ABN90) followed by secondary antibodies incubation for 2 hours at RT (Alexa Fluor™ 488, ThermoFischer, # A-11006, Alexa Fluor™ 647, ThermoFischer, # A-21245, Alexa Fluor™ 555, ThermoFischer, # A-21435). After mounting, slides were imaged at 10X magnification using Slide Scanner microscope (Olympus VS120).

Statistical analysis

Mean and standard deviation were used for statistical analysis in quantifying the effect of different design variables on the system performance, whereas the minimum and the maximum as a shaded area in visualizing the range of system response to a given input (such as compression on the brain in **Fig. 3C** or electrical impedance in **Fig. 4E**). One-way analysis of variance (ANOVA) with post-hoc Tukey's HSD test was performed using Origin 2022 (OriginLab Corp.), when estimating a statistical significance depending on more than two groups of a parameter. The statistical significance was determined using p -values and a value higher than 0.05 ($p > 0.05$) was considered statistically significant ($*p < 0.05$ and $**p < 0.01$). The ANOVA results were reported in figure legends using the following format " $F(dfB, dfW) = F$ -statistic, $p = p$ -value", where dfB and dfW are degrees of freedom between groups and degrees of freedom within groups, respectively.

Supplementary Materials

Fabrication methods.

Experimental methods.

Supplementary Figure S1 – S12.

Supplementary Table S1.

Supplementary Movie S1 – S6.

References

1. A. Palmieri, The concept of the epileptogenic zone: a modern look at Penfield and Jasper's views on the role of interictal spikes. *Epileptic Disorders* **8**, 10–15 (2006).
2. J. P. Mullin, D. Sexton, S. Al-Omar, W. Bingaman, J. Gonzalez-Martinez, Outcomes of Subdural Grid Electrode Monitoring in the Stereoelectroencephalography Era. *World Neurosurgery* **89**, 255–258 (2016).

3. P. C. De Witt Hamer, S. G. Robles, A. H. Zwinderman, H. Duffau, M. S. Berger, Impact of Intraoperative Stimulation Brain Mapping on Glioma Surgery Outcome: A Meta-Analysis. *Journal of Clinical Oncology* **30**, 2559–2565 (2012).
4. J. A. Hartings *et al.*, Direct current electrocorticography for clinical neuromonitoring of spreading depolarizations. *Journal of Cerebral Blood Flow & Metabolism* **37**, 1857–1870 (2016).
5. D. De Ridder, G. De Mulder, T. Menovsky, S. Sunaert, S. Kovacs, Electrical stimulation of auditory and somatosensory cortices for treatment of tinnitus and pain. *Prog Brain Res* **166**, 377–388 (2007).
6. M. Lauritzen *et al.*, Clinical Relevance of Cortical Spreading Depression in Neurological Disorders: Migraine, Malignant Stroke, Subarachnoid and Intracranial Hemorrhage, and Traumatic Brain Injury. *Journal of Cerebral Blood Flow & Metabolism* **31**, 17–35 (2010).
7. R. P. Lesser, N. E. Crone, W. R. S. Webber, Subdural electrodes. *Clinical Neurophysiology* **121**, 1376–1392 (2010).
8. J. C. Bulacio *et al.*, Long-term seizure outcome after resective surgery in patients evaluated with intracranial electrodes. *Epilepsia* **53**, 1722–1730 (2012).
9. G. Nune *et al.*, Treatment of drug-resistant epilepsy in patients with periventricular nodular heterotopia using RNS® System: Efficacy and description of chronic electrophysiological recordings. *Clinical Neurophysiology* **130**, 1196–1207 (2019).
10. M. J. Vansteensel *et al.*, Fully Implanted Brain–Computer Interface in a Locked-In Patient with ALS. *New England Journal of Medicine* **375**, 2060–2066 (2016).
11. W. Wang *et al.*, An Electrocorticographic Brain Interface in an Individual with Tetraplegia. *Journal of Neurology* **8**, e55344 (2013).
12. J.-J. Mo *et al.*, Motor cortex stimulation: a systematic literature-based analysis of effectiveness and case series experience. *BMC Neurology* **19**, 48 (2019).
13. J. G. Makin, D. A. Moses, E. F. Chang, Machine translation of cortical activity to text with an encoder–decoder framework. *Nature Neuroscience* **23**, 575–582 (2020).
14. P. D. Marasco *et al.*, Neurorobotic fusion of prosthetic touch, kinesthesia, and movement in bionic upper limbs promotes intrinsic brain behaviors. *Science Robotics* **6**, eabf3368 (2021).
15. D. Y. Chung, F. Oka, C. Ayata, Spreading Depolarizations: A Therapeutic Target Against Delayed Cerebral Ischemia After Subarachnoid Hemorrhage. *Journal of Clinical Neurophysiology* **33**, 196–202 (2016).
16. J. A. Hartings *et al.*, Spreading depolarisations and outcome after traumatic brain injury: a prospective observational study. *The Lancet Neurology* **10**, 1058–1064 (2011).
17. T. Kaiju *et al.*, High Spatiotemporal Resolution ECoG Recording of Somatosensory Evoked Potentials with Flexible Micro-Electrode Arrays. *Front Neural Circuits* **11**, 20 (2017).
18. M. J. Mack, Minimally Invasive and Robotic Surgery. *JAMA* **285**, 568–572 (2001).
19. S. R. Dashti *et al.*, Operative intracranial infection following craniotomy. *FOC* **24**, E10 (2008).
20. J. T. Cole *et al.*, Craniotomy: true sham for traumatic brain injury, or a sham of a sham? *J Neurotrauma* **28**, 359–369 (2011).
21. C. Lin, X. Zhao, H. Sun, Analysis on the risk factors of intracranial infection secondary to traumatic brain injury. *Chinese Journal of Traumatology* **18**, 81–83 (2015).
22. J. Parvizi, S. Kastner, Promises and limitations of human intracranial electroencephalography. *Nature Neuroscience* **21**, 474–483 (2018).
23. J. D. Greer, T. K. Morimoto, A. M. Okamura, E. W. Hawkes, A Soft, Steerable Continuum Robot That Grows via Tip Extension. *Soft Robotics* **6**, 95–108 (2018).
24. I. R. Mineev *et al.*, Electronic dura mater for long-term multimodal neural interfaces. *Science* **347**, 159–163 (2015).
25. I. W. Scudamore, B. C. Dunphy, I. D. Cooke, Outpatient fallopscopy; intra-luminal imaging of the fallopian tube by trans-uterine fibre-optic endoscopy as an outpatient procedure. *BJOG: An International Journal of Obstetrics & Gynaecology* **99**, 829–835 (1992).

26. J. Hepp, A. Badri-Spröwitz, A Novel Spider-Inspired Rotary-Rolling Diaphragm Actuator with Linear Torque Characteristic and High Mechanical Efficiency. *Soft Robotics* **9**, 364–375 (2021).
27. N. D. Naclerio *et al.*, Controlling subterranean forces enables a fast, steerable, burrowing soft robot. *Science Robotics* **6**, eabe2922 (2021).
28. J. Luong *et al.*, Eversion and Retraction of a Soft Robot Towards the Exploration of Coral Reefs. *2019 2nd IEEE International Conference on Soft Robotics (RoboSoft)*, 801–807 (2019).
29. E. W. Hawkes, L. H. Blumenschein, J. D. Greer, A. M. Okamura, A soft robot that navigates its environment through growth. *Science Robotics* **2**, eaan3028 (2017).
30. N. D. Naclerio, C. M. Hubicki, Y. O. Aydin, D. I. Goldman, E. W. Hawkes, Soft Robotic Burrowing Device with Tip-Extension and Granular Fluidization. *2018 IEEE/RSJ International Conference on Intelligent Robots and Systems (IROS)*, 5918–5923 (2018).
31. G. Schiavone *et al.*, Soft, Implantable Bioelectronic Interfaces for Translational Research. *Advanced Materials* **32**, 1906512 (2020).
32. S. P. Lacour, D. Chan, S. Wagner, T. Li, Z. Suo, Mechanisms of reversible stretchability of thin metal films on elastomeric substrates. *Applied Physics Letters* **88**, 204103 (2006).
33. I. R. Mineev, N. Wenger, G. Courtine, S. P. Lacour, Research Update: Platinum-elastomer mesocomposite as neural electrode coating. *APL Materials* **3**, 014701 (2015).
34. H. O. Michaud, J. Teixidor, S. P. Lacour, Soft metal constructs for large strain sensor membrane. *Smart Materials and Structures* **24**, 035020 (2015).
35. V. Normand, D. L. Lootens, E. Amici, K. P. Plucknett, P. Aymard, New Insight into Agarose Gel Mechanical Properties. *Biomacromolecules* **1**, 730–738 (2000).
36. J. Blaber, B. Adair, A. Antoniou, Ncorr: Open-Source 2D Digital Image Correlation Matlab Software. *Experimental Mechanics* **55**, 1105–1122 (2015).
37. P. Sauleau, E. Lapouble, D. Val-Laillet, C. H. Malbert, The pig model in brain imaging and neurosurgery. *animal* **3**, 1138–1151 (2009).
38. F. Meinert *et al.*, Subdural Placement of Electrocorticographic Electrode Array Through a Burr Hole Exposure: 2-Dimensional Operative Video. *Operative Neurosurgery* **23**, e169 (2022).
39. M. M. Swindle, A. Makin, A. J. Herron, F. J. Clubb Jr, K. S. Frazier, Swine as Models in Biomedical Research and Toxicology Testing. *Veterinary Pathology* **49**, 344–356 (2011).
40. M. Gierthmuehlen *et al.*, Evaluation of μ ECoG electrode arrays in the minipig: Experimental procedure and neurosurgical approach. *Journal of Neuroscience Methods* **202**, 77–86 (2011).
41. F. Fallegger *et al.*, MRI-Compatible and Conformal Electrocorticography Grids for Translational Research. *Advanced Science* **8**, 2003761 (2021).
42. U.-J. Jeong *et al.*, A minimally invasive flexible electrode array for simultaneous recording of ECoG signals from multiple brain regions. *Lab on a Chip* **21**, 2383–2397 (2021).
43. M. A. O'Reilly, A. Muller, K. Hynynen, Ultrasound Insertion Loss of Rat Parietal Bone Appears to Be Proportional to Animal Mass at Submegahertz Frequencies. *Ultrasound in Medicine & Biology* **37**, 1930–1937 (2011).
44. E. M. Lillie, J. E. Urban, S. K. Lynch, A. A. Weaver, J. D. Stitzel, Evaluation of Skull Cortical Thickness Changes With Age and Sex From Computed Tomography Scans. *J Bone Miner Res* **31**, 299–307 (2016).
45. B. J. Woodington *et al.*, Electronics with shape actuation for minimally invasive spinal cord stimulation. *Science Advances* **7**, eabg7833 (2021).
46. Z. Li, H. Yang, G. Wang, X. Han, S. Zhang, Compressive properties and constitutive modeling of different regions of 8-week-old pediatric porcine brain under large strain and wide strain rates. *Journal of the Mechanical Behavior of Biomedical Materials* **89**, 122–131 (2019).
47. S. Budday, T. C. Ovaert, G. A. Holzapfel, P. Steinmann, E. Kuhl, Fifty Shades of Brain: A Review on the Mechanical Testing and Modeling of Brain Tissue. *Archives of Computational Methods in Engineering* **27**, 1187–1230 (2020).
48. I. Terem *et al.*, Revealing sub-voxel motions of brain tissue using phase-based amplified MRI (aMRI). *Magn Reson Med* **80**, 2549–2559 (2018).
49. S. Wurth *et al.*, Long-term usability and bio-integration of polyimide-based intra-neural stimulating electrodes. *Biomaterials* **122**, 114–129 (2017).

50. A. D. Degenhart *et al.*, Histological evaluation of a chronically-implanted electrocorticographic electrode grid in a non-human primate. *Journal of Neural Engineering* **13**, 046019 (2016).
51. A. Lecomte, E. Descamps, C. Bergaud, A review on mechanical considerations for chronically-implanted neural probes. **15**, 031001 (2018).
52. S. Emich, M. Dollenz, Burr hole is not burr hole: technical considerations to the evacuation of chronic subdural hematomas. *Acta Neurochirurgica* **157**, 497–499 (2015).
53. L. Dejace, H. Chen, I. Furfaro, G. Schiavone, S. P. Lacour, Microscale Liquid Metal Conductors for Stretchable and Transparent Electronics. *Adv Mater Technol*, 2100690 (2021).
54. Y.-L. Park, B.-R. Chen, R. J. Wood, Design and Fabrication of Soft Artificial Skin Using Embedded Microchannels and Liquid Conductors. *IEEE Sensors Journal* **12**, 2711–2718 (2012).
55. M. A. Robertson, L. Dejace, S. P. Lacour, J. Paik, Bi-modal control of vacuum-powered soft pneumatic actuators with embedded liquid metal-based strain sensitive skin. *2019 2nd IEEE International Conference on Soft Robotics (RoboSoft)*, 217–221 (2019).
56. L. Dejace, N. Laubeuf, I. Furfaro, S. P. Lacour, Gallium-Based Thin Films for Wearable Human Motion Sensors. *Adv Intell Syst* **1**, 1900079 (2019).
57. A. P. Gerratt, H. O. Michaud, S. P. Lacour, Elastomeric Electronic Skin for Prosthetic Tactile Sensation. *Advanced Functional Materials* **25**, 2287–2295 (2015).
58. J. Viventi *et al.*, Flexible, foldable, actively multiplexed, high-density electrode array for mapping brain activity in vivo. *Nature Neuroscience* **14**, 1599–1605 (2011).
59. F. Fallegger, G. Schiavone, S. P. Lacour, Conformable Hybrid Systems for Implantable Bioelectronic Interfaces. *Advanced Materials* **32**, 1903904 (2020).
60. L. Xu *et al.*, 3D multifunctional integumentary membranes for spatiotemporal cardiac measurements and stimulation across the entire epicardium. *Nature Communications* **5**, 3329 (2014).
61. D.-H. Kim *et al.*, Dissolvable films of silk fibroin for ultrathin conformal bio-integrated electronics. *Nature Materials* **9**, 511–517 (2010).
62. C. M. Tringides *et al.*, Viscoelastic surface electrode arrays to interface with viscoelastic tissues. *Nature Nanotechnology*, 1–11 (2021).
63. C. P. Teuwen, C. Kik, P. Knops, Quantification of the Arrhythmogenic Effects of Spontaneous Atrial Extrasystole Using High-Resolution Epicardial Mapping. *Circulation: Arrhythmia and Electrophysiology* **11**, e005745 (2018).
64. A. Farajidavar, Bioelectronics for mapping gut activity. *Brain Research* **1693**, 169–173 (2018).
65. L. Miller, A. Farajidavar, A. Vegesna, Use of Bioelectronics in the Gastrointestinal Tract. *Cold Spring Harbor Perspectives in Medicine* **9** (2019).
66. M. Capogrosso *et al.*, A brain–spine interface alleviating gait deficits after spinal cord injury in primates. *Nature* **539**, 284–288 (2016).
67. T. Trantidou, Y. Elani, E. Parsons, O. Ces, Hydrophilic surface modification of PDMS for droplet microfluidics using a simple, quick, and robust method via PVA deposition. *Microsystems & Nanoengineering* **3**, 3461 (2017).

Acknowledgments: the authors would like to thank Ivan Furfaro in the Laboratory for Soft Bioelectronic Interfaces (LSBI) for building the experimental set-up with a customized code for the track resistance change measurements, Michael Shur (LSBI) for his technical support on measuring the inflation of the deployable ECoG strips, Emilie Revol (LSBI) for her assistance in the acute recording of a mini pig’s brain; the Neurosoft Bioelectronics team (Nicolas Vachicouras, Ludovic Serex, Benoit Huguet) for insightful comments on the design and manufacturing of soft microelectrode arrays; the Neural Microsystems Platform staff at FCBG (Valerian Ruhaut, Anthony Guillet, and Michael Stoeckel) for their help and support and the medical staff at the Geneva University Hospital for their technical support during the surgery. Finally, all authors show their best gratitude to all team members in the LSBI for their countless support, help and discussion throughout the project, which were critical in achieving the results presented in this paper. **Funding:** SNSF Bridge grant to F.F.; the Bertarelli Foundation,

Innosuisse project 41945.1 IP-LS, SNSF Sinergia CRSII5_183519, and the Wyss Center grant (WCP 015 Soft ECoG)⁷ to S.P.L. **Author contributions:** S.S. and S.P.L. designed the study and experiments. S.S. designed the device and fabrication process. S.S. and F.F. performed prototyping. S.S. performed the *in-vitro* experiments and analyzed the data. K.K. performed the FEM analysis. F.F. and A.T. performed the *in-vivo* brain recording of a mini pig and analyzed the brain recording data. All authors contributed to the redaction and proofreading of the manuscript. **Competing interests:** A patent application on this deployment system was filed by the École polytechnique fédérale de Lausanne (EPFL). F.F. and S.P.L. are co-founders of Neurosoft Bioelectronics SA that may exploit the aforementioned patent application. **Data and materials availability:** All data needed to evaluate the conclusions in the paper are present in the Main manuscript and Supplementary Materials. Additional data can be provided upon request. The datasets generated and analyzed in the current study are available at Zenodo (<https://doi.org/10.5281/zenodo.7807013>).

ACCEPTED

Figures

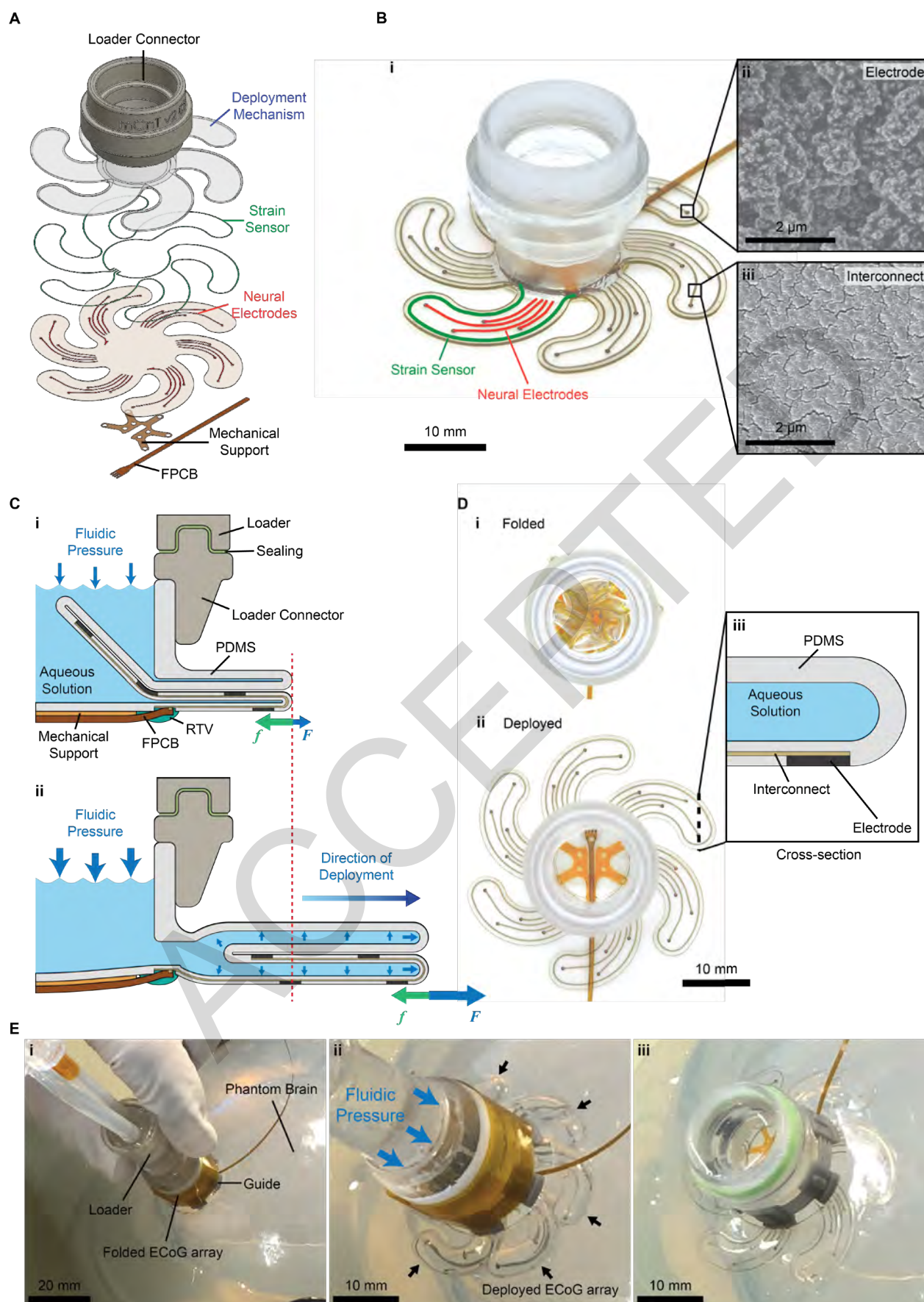


Fig. 1 | Design, fabrication and working principle of the deployable ECoG system. (A) A breakdown image of a multi-legged deployable ECoG array consisting of everting actuation mechanism, strain sensor and surface electrodes. (B) Photographic images of the ECoG array prototype: (i) an overview, (ii) a scanning electro-microscope (SEM) image of Pt-PDMS

composite and (iii) a SEM image of microcracked gold thin-film interconnect. (C) Schematic cross-sections of the deployable ECoG system: (i) folded and (ii) deployment with a positive fluidic pressure differential. A red dashed line indicates the initial position of the leg before deployment. F and f indicate fluidic force and friction, respectively. (D) Photographic top views of the ECoG array prototype: (i) folded and (ii) fully deployed. (iii) A schematic cross-section of the ECoG array showing its air-pocket structure filled with aqueous solution as a lubricant. (E) Photographic images of the ECoG prototype being deployed in a phantom brain model: (i) positioning a folded system in a burr hole (22 mm in diameter) of the synthetic phantom brain consisting of a hydrogel block and a plastic skull, (ii) deploying the system with a positive fluidic pressure differential (arrows indicate deployed electrode arrays) and (iii) removing a loader to leave the deployed ECoG in position.

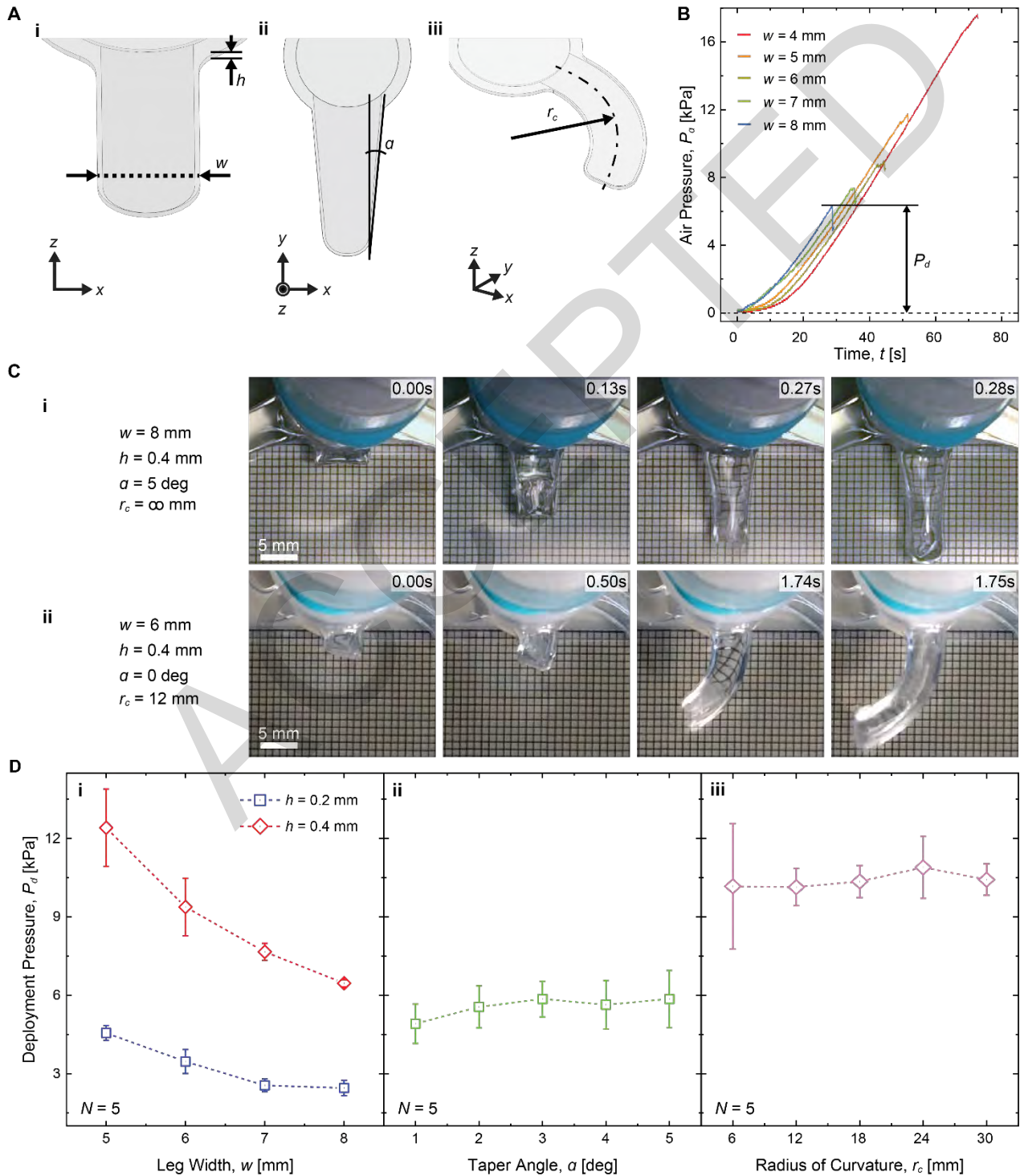


Fig. 2 | Deployability of the actuated ECoG legs (A) 3D images of tested legs: (i) a straight leg with width w and thickness h , (ii) a tapered leg with taper angle a , and (iii) a curved leg with radius of curvature r_c . (B) Profiles of air pressure P_a inside straight legs with respect to time t , depending on different width w . By default, $h = 0.4$ mm, $a = 0$ deg, and $r_c = \infty$ mm. (C) Sequential images of deployment of leg strips, (i) a tapered leg and (ii) a curved leg. w , h , a , and r_c are described in the image. (D) Deployment pressure P_d depending on various design variables: (i) leg width w and thickness h , (ii) taper angle a , and (iii) radius of curvature r_c . Statistical analysis (One-way ANOVA test) reveals that there is no statistical significance in P_d with respect to a change in a ($F(4, 20) = 1.01$, $p = 0.42$) and r_c ($F(4, 20) = 0.27$, $p = 0.89$). By default, $h = 0.4$ mm, $w = 6$ mm, $a = 0$ deg, and $r_c = \infty$ mm. Each data point in D is an average of five different measurements ($N = 5$) with a single specimen. Error bars indicate \pm SD (standard deviation).

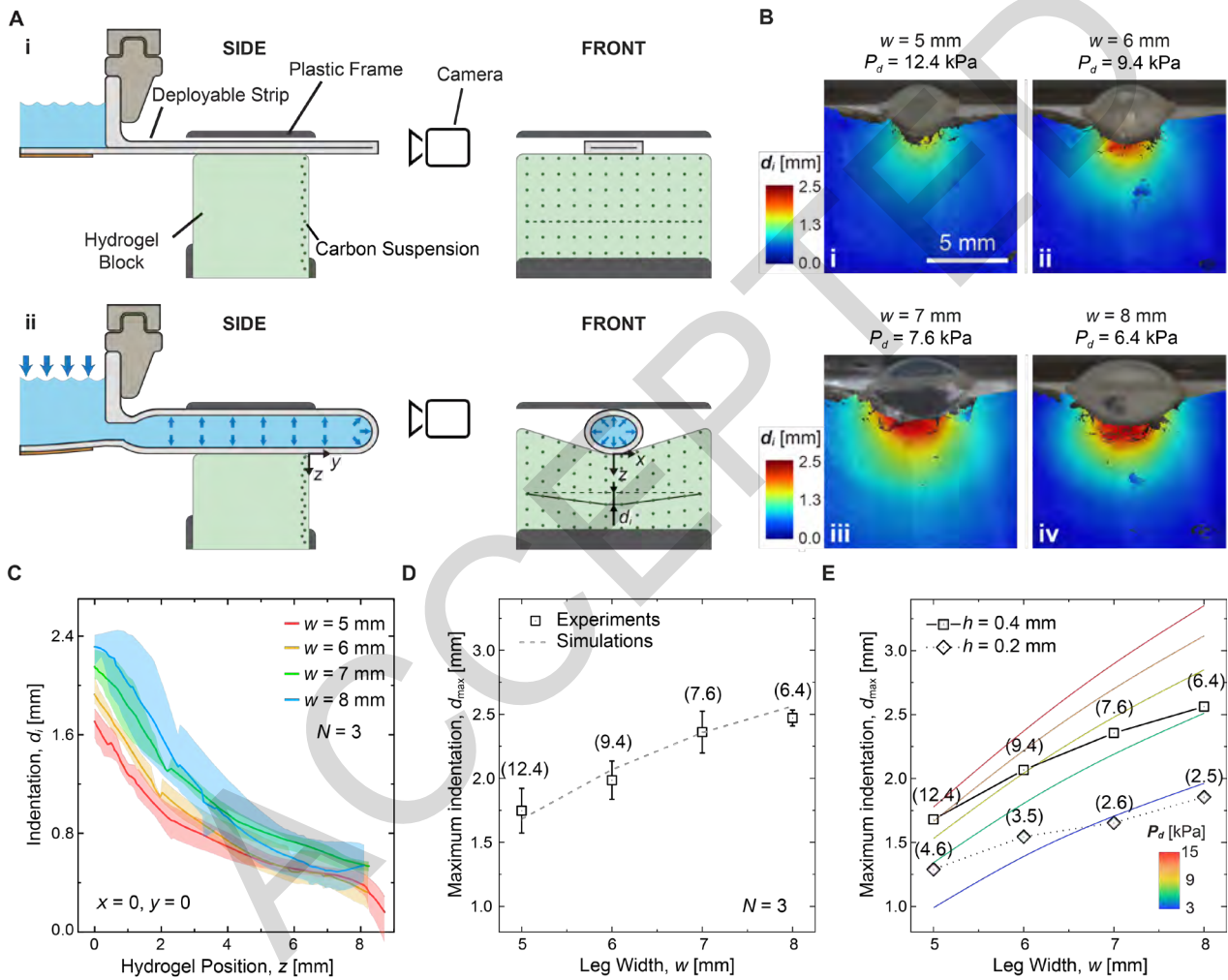


Fig. 3 | Indentation of a phantom brain depending on various deployable ECoG leg shapes (A) A schematic side- and front-view of a single straight leg ($h = 0.4$ mm and $a = 0$ deg) with experimental set-up (i) before and (ii) after pressurization. The central axis of the leg is taken as the initial reference ($x = y = z = 0$). The indentation d_i is on the boundary between the bottom of the inflated leg and the hydrogel block in the final deformed configuration. Note that the actual carbon suspension is randomly dispersed on the hydrogel surface. (B) Color maps of d_i of the hydrogel block indented by the leg with different w : (i) $w = 5$ mm, (ii) $w = 6$ mm, (iii) $w = 7$ mm and (iv) $w = 8$ mm. Each leg design is inflated with its corresponding P_d shown in Fig. 2D-i. (C) Profiles of d_i with respect to z depending on different w . Each solid line is an average of three measurements ($N = 3$) using the same leg sample. Shaded areas show a range of the minimum and the maximum d_i . (D) Maximum indentation d_{max} of various leg shapes with different w when inflated with its corresponding P_d . Each data point is an average of three

different measurements ($N = 3$) using the same leg sample. Error bars indicate \pm SD. Dashed line represents data from calculations of the FEM model. **(E)** Numerical estimation on d_{\max} of various leg shapes with different w , h , and P_d . The dashed line and colored solid lines are d_{\max} for the leg with $h = 0.4$ mm and $h = 0.2$ mm, respectively. Numbers in the brackets in **D** and **E** are corresponding P_d for the given w and h .

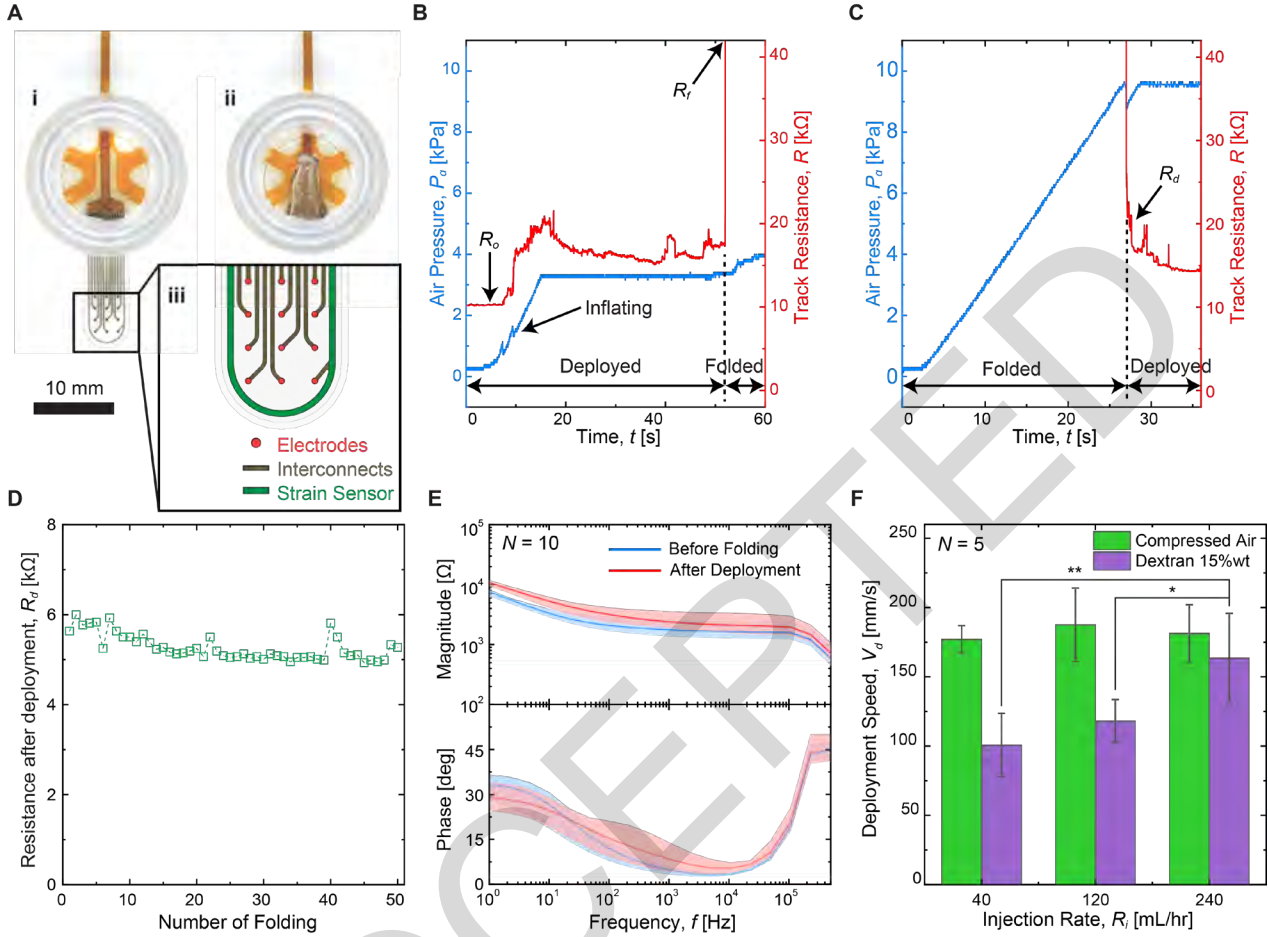


Fig. 4 | Functional verification of the deployable ECoG system (A) Photographs of the top views of a deployable ECoG array (single straight leg prototype): (i) deployed and (ii) folded. (iii) A layout of electrodes, interconnects, and strain sensor. (B) Profiles of internal air pressure P_a and track resistance R of strain sensor with respect to time t during folding and (C) deployment. R_o , R_f , and R_d indicate the initial track resistance before folding, track resistance after folding, and track resistance after deployment, respectively. (D) Track resistance after deployment R_d with respect to the number of folding. (E) Electrochemical impedance magnitude (top) and phase (bottom) of 10 channels ($N = 10$) on the functional deployable ECoG array before folding (blue) and after deployment (red) as a function of frequency. Shaded areas show a range of the minimum and the maximum phase and magnitude. (F) Deployment speed V_d of the deployable strip filled with different fluids as a function of injection rate R_i . Each data point is an average of five different measurements ($N = 5$) using the same strip sample. Error bars indicate \pm SD. Statistical analysis (One-way ANOVA test) reveals that there is no statistical significance in V_d depending on R_i for the compressed air ($F(2, 12) = 0.35$, $p = 0.71$), unlike the case of aqueous solution (Dextran 15% wt) ($F(2, 12) = 8.87$, $p = 0.004$). * and ** indicate $p < 0.05$ and $p < 0.01$, respectively.

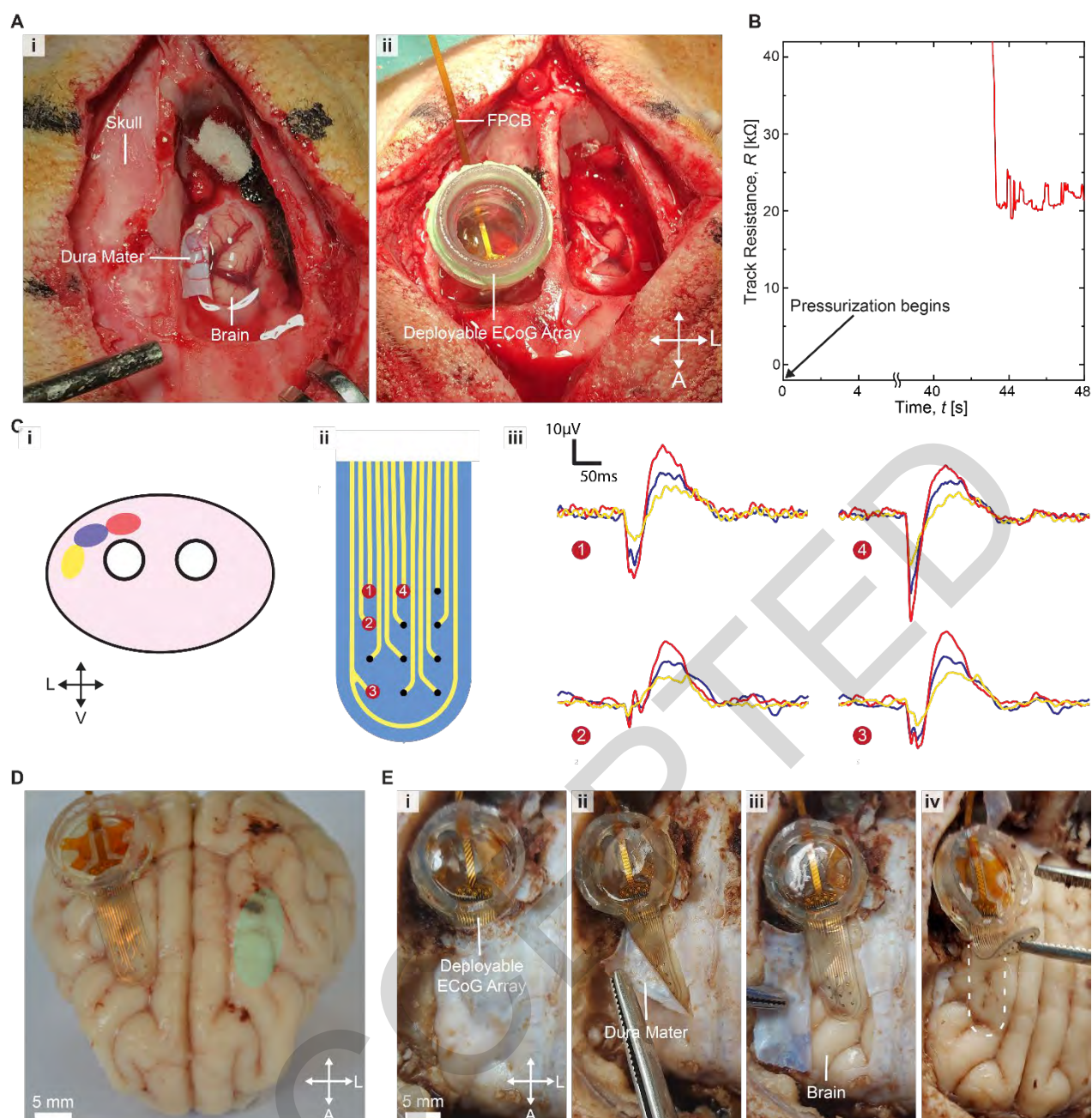


Fig. 5 | In-vivo acute recording of SSEPs in a minipig model (A) Surgical access for the deployment of the soft robotic ECoG array on the brain: (i) overview of the access to the brain, (ii) ECoG system after placement on the brain. **(B)** Changes in the electrical track resistance of the strain sensor during the deployment procedure. **(C)** Recording of the SSEPs on the brain after deployment of the ECoG array: (i) location of the three placements of stimulation on the snout, (ii) electrode design, and (iii) SSEPs from the snout stimulation according to the snout stimulation position (color codes match with C-i). **(D)** Photograph of the extracted brain with the position of the electrode array depicted in green on the contralateral hemisphere. **(E)** Extraction of the ECoG array following the brain perfusion showing the deployed soft array. The dashed line in iv overlaps with the area initially covered by the deployable ECoG strip.